JGR Atmospheres

RESEARCH ARTICLE
10.1029/2024JD043194

Effects of Ocean Heat Transport in Tropical Radiative Convective Equilibrium

B. D. Dygert[1] and **Dennis L. Hartmann**[1]

[1]Department of Atmospheric and Climate Science, University of Washington, Seattle, WA, USA

Key Points:

- For temperatures similar to the current tropics, ocean heat transport cools the climate by increasing the efficiency of longwave cooling
- A cold high-temperature-contrast climate driven by low clouds transitions abruptly to a warmer low-contrast climate with fewer low clouds
- The transition to more sensitive climates above 310 K is not affected by the presence of ocean heat transport

Correspondence to:
B. D. Dygert,
bdygert@uw.edu

Citation:
Dygert, B. D., & Hartmann, D. L. (2025). Effects of ocean heat transport in tropical radiative convective equilibrium. *Journal of Geophysical Research: Atmospheres*, *130*, e2024JD043194. https://doi.org/10.1029/2024JD043194

Received 19 DEC 2024
Accepted 9 JUL 2025

Abstract A global climate model is run in radiative-convective equilibrium including a slab ocean with a specified ocean heat transport analogous to what is seen in the tropical Pacific. The insolation is varied to create a range of global mean equilibrium temperatures. These results are compared with experiments that do not include a specified ocean heat transport. The ocean heat transport cools the coldest Sea Surface Temperatures (SSTs) and increases the SST contrast. The warmest SSTs change much less with the addition of ocean heat transport because increased atmospheric transport moves energy away from the warm region. The ocean heat transport also increases the efficiency of cooling by outgoing longwave radiation in the subsiding region, allowing for a cooler global mean SST. At colder global mean temperatures ocean heat transport creates a high-contrast state in which abundant low clouds play a strong role in maintaining the SST contrast. This high-contrast state abruptly transitions to a warmer, low-SST-contrast state as the climate is warmed by increasing insolation. At warmer temperatures comparable to the current tropics, the low cloud response is less important than longwave emission in maintaining the SST contrast. Although ocean heat transport cools the climate, it does not much affect the sensitivity of the model climate to increasing insolation. Comparison of the model results to ERA5 reanalysis data shows that mechanisms responsible for the SST distribution and energy budget changes in this idealized model are analogous to variability that occurs over the tropical Pacific Ocean.

Plain Language Summary Using an idealized model, we study the effect of the transport of energy by tropical ocean on the overall climate. In general, tropical ocean heat transport cools the climate by influencing the atmospheric circulation and structure. For sea surface temperatures most likely the current Tropics, ocean heat transport helps the climate cool more efficiently through its effect on the distribution of water vapor in the atmosphere. For colder sea surface temperatures, the ocean heat transport leads to more low clouds over the cooler water, which then play a larger role in cooling the climate. This role for low clouds is reduced when the climate is warmed. Although our experiment is much simpler than the real world, we find analogous behavior when comparing to the observed changes associated with El Niño Southern Oscillation variations.

1. Introduction

The spatial pattern of Sea Surface Temperature (SST) in the tropics plays an important role in the mean climate and its sensitivity to change. For example, the circulation of the atmosphere responds strongly to changes in the tropical SST distribution (Bjerknes, 1966; Horel & Wallace, 1981). The separation of the circulation into regions of rising and sinking motion affects the outgoing longwave radiation (OLR). Regions of subsidence have lower water vapor content and form regions where the OLR is greater for a given SST than regions with higher humidity. This separation into regions of efficient longwave radiation to space and less efficient longwave radiation to space decreases the sensitivity of climate (Pierrehumbert, 1995).

The SST gradient also affects the abundance and optical properties of low clouds that form in regions of lowered SST and increased lower tropospheric stability (Klein & Hartmann, 1993). Increases in tropical SST gradient can increase the low cloud fraction in the cold SST region through both thermodynamic and dynamic effects, which may lead to a negative climate feedback (Bretherton & Blossey, 2014; Larson et al., 1999; Miller, 1997).

Recent work has shown that an increase in the tropical SST contrast in the past 40 years has led to a negative "pattern effect" on climate sensitivity, primarily by increasing the reflectivity of low clouds over the cooler SST (Andrews et al., 2018; Armour, 2017; Dong et al., 2020; Stevens et al., 2016; Zhou et al., 2016). The La Niña-like SST changes in the tropical Pacific (warming in the West Pacific and cooling in the East Pacific) has global radiative effects that can lead to a lower apparent climate sensitivity (Armour et al., 2024; Dong et al., 2019).

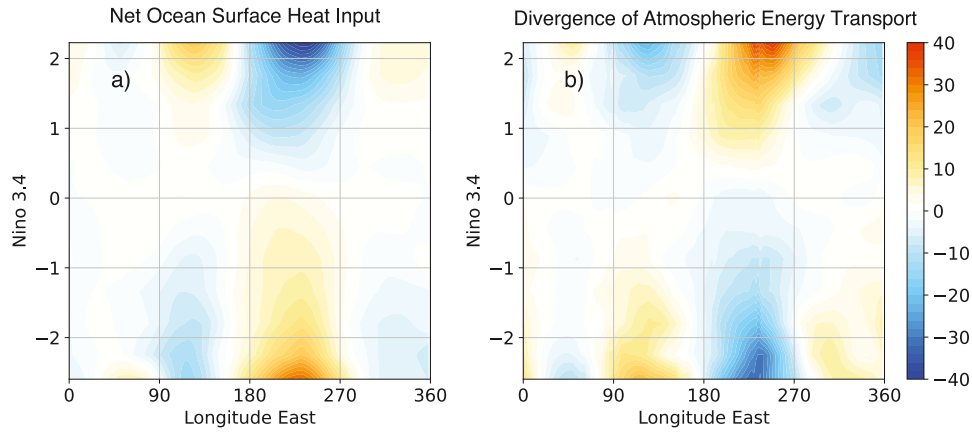

Figure 1. Contour plot of (a) anomalous net flux of heat into the ocean and (b) divergence of total energy transport by the atmosphere averaged for the region from 10S to 10N as functions longitude and Niño 3.4 anomaly. Data are from ERA5. Units are Wm^{-2}.

To better understand the mechanisms connecting the SST pattern and radiation and how these might change with warming, it is helpful to study these interactions in a simplified framework. One method of studying the interactions between clouds, large-scale circulation and climate in a simplified framework is global radiative convective equilibrium (RCE) calculations in which the atmospheric structure is determined by a balance between radiative cooling and convective heating. Simulations over a fixed and uniform SST show that at high enough temperatures the circulation organizes into regions of moist air and convection and regions of dry air and subsidence, a process often called self-aggregation (Bretherton et al., 2005; Coppin & Bony, 2015; Cronin & Wing, 2017; Held et al., 1993, 2007; Retsch et al., 2019; Tompkins, 2001). The initialization of self-aggregation in these uniform and fixed SST experiments is highly dependent on both the surface fluxes and the radiative cooling rates, and the dominant mechanism responsible can vary with the SST value (Bretherton et al., 2005; Coppin & Bony, 2015).

Aggregation of convection causes organization of the surface energy fluxes, with more column and surface energy loss over the dry subsiding region than over the warm rising region. One is then motivated to consider a model in which the SST can respond to these changed energy fluxes and allow the SST gradients to obtain their natural balance. A simple way to do this is to introduce a prediction equation for the SST, which assumes the surface is wet and has a heat capacity corresponding to a fixed depth of seawater, often called a slab ocean model. In this case a significant time-mean SST contrast develops, whose magnitude may also oscillate in time accompanied by an oscillation in the degree of aggregation (Coppin & Bony, 2018; Dygert & Hartmann, 2023; Popke et al., 2013; Reed & Chavas, 2015). Hartmann and Dygert (2022) found that when forced by changing global mean insolation, such an RCE calculation with a slab ocean model in a global domain showed a change in apparent climate sensitivity from higher sensitivity for low global mean SST, low sensitivity for intermediate SST comparable to the current climate, and higher sensitivities for temperatures greater than about 310 K. The transition to larger sensitivity around 310 K has been reported in prior studies (Meraner et al., 2013; Russell et al., 2013).

In the present study, we wish to know how the above considerations concerning RCE above a slab ocean would be changed by ocean heat transport. For example, does the addition of ocean heat transport change the mean climate or its variations? Does the introduction of ocean heat transport change the sensitivity of climate? If either of these changes occur, by what mechanisms are these changes produced?

To make these considerations a little less abstract, we can think of these idealized experiments as a partial analog to the Walker Circulation. Then, let us consider the cases of El Niño Southern Oscillation (ENSO) variations in the tropical Pacific, where the mean state and its variations are affected by oceanic energy transport. Figure 1 shows the anomalous net energy flux from the atmosphere into the ocean and the total energy flux divergence in the atmosphere as functions of longitude and Niño 3.4 index. Data were obtained from ERA5 reanalysis (Hersbach

et al., 2020). The Niño 3.4 index was computed from the ERA5 SST averaged over the region 5°N–5°S, 190°E−240°E.

Figure 1a shows that during a strong El Niño event (Niño 3.4 ≈ +2) there is an anomalous flux of nearly 40 Wm^{-2} from the ocean to the atmosphere in the Eastern Pacific equatorial ocean. These anomalies in surface heat flux are formed of about equal parts increased surface evaporation and decreased absorbed solar radiation anomalies (not shown). Figure 1b shows that a nearly equal flux of energy is carried away from the region by the atmosphere during strong El Niño events. This export of energy results in a convergence of atmospheric energy transport in other equatorial regions, though some is transported to the extratropics. Although the evolution of tropical SST during El Niño events is a transient process, and storage in the ocean is important (Cheng et al., 2019), the time scale is long enough that surface fluxes are in balance with atmospheric transport. In the calculations to be described below we will assume that the ocean heat transport is constant in time and compute the equilibrium response of SST and the associated atmospheric circulation to that constant ocean heat transport.

To represent the effect of ocean heat transport in the context of our global RCE model with a slab ocean, we introduce constant, but spatially varying sources and sinks of energy in the slab ocean. We then compare these simulations with control simulations in which no ocean heat transport is included.

The model and experiment descriptions can be found in Section 2. We then describe the change in the SST distribution between the control and the ocean heat transport experiments in Section 3. Section 3.6 discusses the effect of ocean heat flux on the sensitivity to insolation changes. Finally, in Section 4, we see that the changes in energy budget when adding ocean heat transport to our idealized experiments are similar to the changes we see in observations of the transition from El Niño to La Niña over the tropical Pacific Ocean, although our model experiments are only a very rough analogy to the tropical Pacific and ENSO.

2. Model and Experiments

Experiments are conducted using GFDL's AM2.1 with no rotation, uniform insolation, 50-m slab ocean, no land, 2 by 2.5° horizontal resolution, and 32 vertical levels. Stated differently, this is an aqua-planet simulation with no rotation and uniform insolation, simulating a tropical world. Control experiments are conducted with no ocean heat transport. By increasing the insolation, we create a series of control experiments at a range of global mean SSTs from about 288 to 318 K. Simulations are run long enough to produce a sample of 40 years of equilibrated climate after a spin-up period of 20 or more years. The control experiments with no ocean heat transport are taken from Hartmann and Dygert (2022) and more details about these experiments can be found there.

In this paper, we use the same model configurations as Hartmann and Dygert (2022), except that we apply sources and sinks of energy to the slab ocean layer. In climate modeling that employs slab ocean models, sources and sinks of energy added to mimic the effect of ocean heat transport are often called "Q-fluxes." So, in comparing these cases to the control cases described above, we will use the letter C to denote the control cases without ocean heat transport and we will use the letter Q to denote the new simulations with specified ocean heat transport.

The shape and magnitude of the Q-fluxes were chosen to loosely replicate the natural structure of SST anomalies emerging from the control experiments, which tend to take on a global wavenumber one pattern with one maximum and one minimum (Hartmann & Dygert, 2022). As shown in Figure 2a, we use a Gaussian shaped dipole of Q-flux with a maximum magnitude of 50 Wm^{-2}. The global-mean Q-flux is zero. A value of 50 Wm^{-2} was found to be large enough to lock the convection over the warmest SST. Because convection preferentially occurs over warmer SSTs, positive Q-flux serves as an attractor for the atmosphere to organize around—with convection and warmer SSTs above the positive Q-flux and colder SSTs and subsidence above the negative Q-flux. The magnitude of ocean heat transport chosen here is not too dissimilar from the observed anomalies associated with El Niño shown in Figure 1. Also, the climatological flux of energy into the ocean in the equatorial eastern Pacific is on the order of 100 Wm^{-2} (Hartmann, 2016), which is similar to the contrast in ocean heat transport that we apply here. This magnitude of Q-flux fixes the locations of warm and cold SSTs over the regions of positive and negative Q-flux, respectively. With significantly weaker Q-flux, the internal feedbacks between the atmosphere and the ocean are sufficiently strong to move the SST around in space as in experiments with zero Q-flux. This simplified Q-flux is included to test the reaction of the atmosphere to forcing from the ocean, resembling an idealized version of the gradient in ocean heat uptake from the East Pacific to the West Pacific and Indian Oceans.

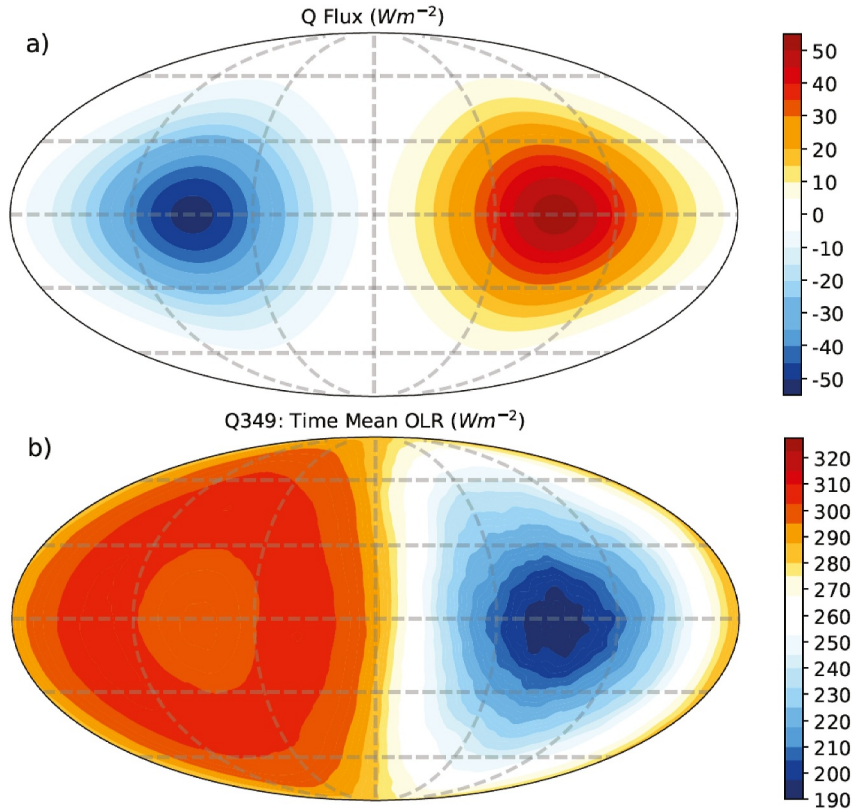

Figure 2. Global structure of (a) time invariant Q Flux and (b) outgoing longwave radiation averaged over the final decade of simulation in Hammer equal-area projection.

As an example of how the atmosphere responds to the imposed Q-flux, Figure 2b shows the time mean OLR. The Q-flux fixes the regions of subsiding and ascending motion over the regions of cooling and warming, respectively, and the OLR reflects the location of convection. The OLR is enhanced over the dry, subsiding region over the region of negative Q-flux, and is suppressed over the region of positive Q-flux where the atmosphere is ascending, moist, and cloudy.

3. Mean State Changes

In this section, we will discuss the changes to the SST distribution and energy budget between cases with and without the Q-flux. Figure 3a shows the SST averaged over the coldest 20% by area, warmest 20% by area and the global mean SST as functions of the insolation for both the control cases and the Q-flux cases. In all cases, the coldest 20% of SST values decreases much more than the warmest 20% of SST values in response to Q-flux, and in every case the global mean temperature is cooled by the addition of Q-flux. The Q-flux has a dramatic effect on SST, except for the SST over the warmest 20% of SST for cases with global mean SST similar to the current tropical climate (≈300–309 K). In these cases, the warmest SST values only decrease by a small amount in response to Q-flux.

The addition of Q-flux has a much larger effect at colder temperatures corresponding to low insolation values, and introduces an apparent abrupt regime transition from a colder to warmer climate when crossing insolation values of about 335 Wm^{-2} (Figure 3a). The reasons for this transition will be discussed later, but it is similar to a much weaker transition in sensitivity and temperature that occurs between a cold regime and an intermediate regime in the control cases (Hartmann & Dygert, 2022). Also apparent is a change to increased sensitivity to insolation increases that occurs around global mean temperature of 310 K. As mentioned previously, many climate models show an increase in climate sensitivity at temperatures around 310 K, which is associated with the increased efficiency of water vapor absorption, particularly in the continuum region (Hartmann & Dygert, 2022; Meraner et al., 2013). This warm transition occurs both in the control and Q-flux cases. Between the cold and warm

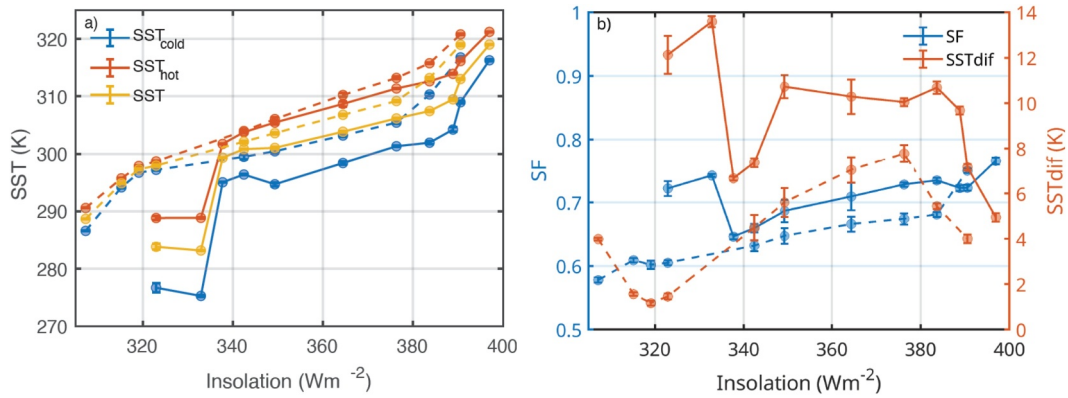

Figure 3. Line plots vs. insolation of (a) the coldest 20% Sea Surface Temperatures (SSTs) (blue), warmest 20% SSTs (red) and global mean SST (yellow) for the Q-flux (solid) and control (dashed) cases, and (b) the SST contrast between the top and bottom 20% SSTs (SSTdif) in orange and the subsiding fraction in blue for the control (dashed) and OHT (solid cases).

transitions is a region of relatively stable climate, as measured by the increase of temperature with increasing insolation. Hartmann and Dygert (2022) showed that this stable region is associated with the strong stabilizing effect of the radiator fin mechanism of Pierrehumbert (1995) in this temperature range.

3.1. SST Distribution and Organization

In simulations with uniform SST the organization in RCE experiments can be characterized by the subsiding fraction (SF), the area of the domain with downward motion (Wing et al., 2017). Here, we compute the SF using the mass-averaged pressure velocity. With predicted SST, however, the SST contrast between the cold and warm regions can also be used as a metric for the strength of self-aggregation. We define this SST contrast, *SSTdif*, as the difference between the warmest and coldest 20% of SSTs. Because there is no rotation and insolation is uniform, in cases with no Q-flux the warm and cold pools do not have any spatial preference and tend to move around with time and oscillate in amplitude (Coppin & Bony, 2017; Dygert & Hartmann, 2023). In the cases with strong Q-flux discussed here, the upward motion tends to remain over the geographically fixed region of positive Q-flux, where the warmest SST values also remain. The water vapor follows the Q-flux and SST distribution. Because the Q-flux tends to fix regions of subsiding and ascending motion in place, the moisture gradient between the two regions is enhanced. The effect of this on the OLR distribution is shown in Figure 2b. The OLR is enhanced in the dry, subsiding region over the coldest SSTs and suppressed in the humid, convecting region over the warmest SSTs.

As shown in Figure 3b, in the control experiments (dashed lines) SST contrast at first declines with increasing SST, up to an SST value of about 300 K, after which it increases up until 310 K at which point it rapidly declines as the climate is warmed further. In the case with Q-flux the SST contrast is very large for the two lowest values of insolation and temperature, then abruptly drops as the insolation is increased further. By comparing Figures 3b and 3a, one can see that the rapid transition in the Q-flux case occurs at about the same global mean temperature of 300 K as the change from decreasing to increasing SST contrast in the control case. For the Q-flux experiments there is also a rapid reduction in the SF as the temperature warms across the rapid transition around 300 K. We force the SST to change with insolation variations, but we believe that the regime transitions would occur at similar temperatures if we forced climate change in a different way, such as increasing carbon dioxide. This is because the regime transitions are related to the amount of water vapor in the atmosphere, which is mostly a function of mean SST.

The SF is shown in Figure 3b. It is greater than 60% in almost all cases and increases in response to Q-flux. Greater SST contrast generally tends to concentrate the convection in a smaller portion of the domain (Dygert & Hartmann, 2023). Subsiding fraction is greater than 70% for the two cold cases and drops significantly as the climate abruptly warms around insolation of 335 Wm^{-2}, where the mean SST increases from about 285 to 300 K in the Q-flux experiments.

To summarize, Q-flux cools the mean climate compared with the control case. Most of this cooling occurs in the subsiding cold region. The climate has three regimes similar to the control case, with an intermediate insensitive climate and cooler and warmer edge climates that are more sensitive. These regimes are shifted to higher insolation values in the Q-flux experiments because of the mean cooling that Q-flux produces. In the Q-flux case, the cold regime is very cold with high SST contrast and shifts abruptly to a warmer climate with much reduced SST contrast as the insolation is increased by a small amount. The mean SST increases from ≈285 K to ≈300 K across this cold transition. The transition to a more sensitive very warm climate occurs at about 310 K for both the Q-flux and control cases, as has been observed in other GCM studies.

3.2. Energy Budget Changes

As in the case of the observed El Niño cycle shown in Figure 1, the atmosphere energy transport will play an important role in the simulations described here. We define the divergence of vertically integrated total energy transport (DAT) as the mass-integrated flux divergence of moist static energy, where V is the horizontal wind field and P is pressure.

$$\mathrm{DAT} = \frac{1}{g}\int_0^{P_s} \nabla \cdot (\mathrm{MSE}\ \mathbf{V})\, dP \tag{1}$$

Assuming atmospheric energy storage is small, however, DAT can alternatively be calculated as a residual in the atmospheric energy budget equation, which becomes the difference in top of the atmosphere radiation and the flux of energy across the surface.

$$\mathrm{DAT} = R_{net,TOA} - \mathrm{SEF} \tag{2}$$

Here, we define the surface energy flux from the atmosphere to the ocean (SEF) as the total of all energy budget terms crossing the surface. The surface flux terms are the net LW at the surface (LW_{net}), the net SW at the surface (SW_{net}), and the surface fluxes associated with evaporation (LE) and sensible heat flux (SH). On average, the surface fluxes are balanced by the imposed Q-flux, as is required by energy conservation.

$$\mathrm{SEF} = LW_{net} + SW_{net} - (\mathrm{LE} + \mathrm{SH}) \tag{3}$$

Figure 4 shows key regional top-of-atmosphere energy budget terms for the regions with mass-averaged upward and downward motion, which correspond to warm and cold regions. Figure 4 panels a and b show top-of-atmosphere energy budget terms for the subsiding and rising regions, respectively, for both the control (dashed) and Q-flux (solid) cases. Note that the divergence of atmospheric energy transport, DAT, is plotted with opposite sign, so that it is actually the convergence of atmospheric energy transport. This is done so that DAT and Q-flux do not obscure each other in the plot. Because these values are averaged over the regions of upward and downward motion, some changes in these values, particularly changes in the atmospheric energy transport, can be attributed to changes in the size of the ascending and descending regions. Looking first at Figure 4a we see that in the downward region a close balance exists between net shortwave absorption and OLR, with the small difference balanced by atmospheric transport and Q-Flux. For the two cold Q-flux cases we see a large reduction in both OLR and net shortwave radiation. The OLR decreases because it is colder in the Q-flux case than in the control case, and it is colder because the absorbed solar radiation is less, which we will see is associated with increased low cloud reflectivity.

Turning to the region of rising motion in Figure 4b, we see that the OLR is again substantially reduced for the two coldest cases, again because it is colder, but the net solar radiation is not correspondingly decreased, since in the rising region high clouds are always present. The albedo of the high clouds in the upward region does not respond much to the addition of Q-flux. In the rising region the increase in the TOA radiation balance that would be implied by the reduction in OLR is balanced by an increase in the divergence of atmospheric energy transport, DAT.

Figures 4c and 4d show the changes in energy budget components between the Q-flux and control experiments for each insolation value. DAT and OLR are shown with negative signs to indicate their effect on the TOA energy budget. Let us begin by discussing the coldest cases, with insolation equal to 323 and 333 Wm^{-2}, respectively. In

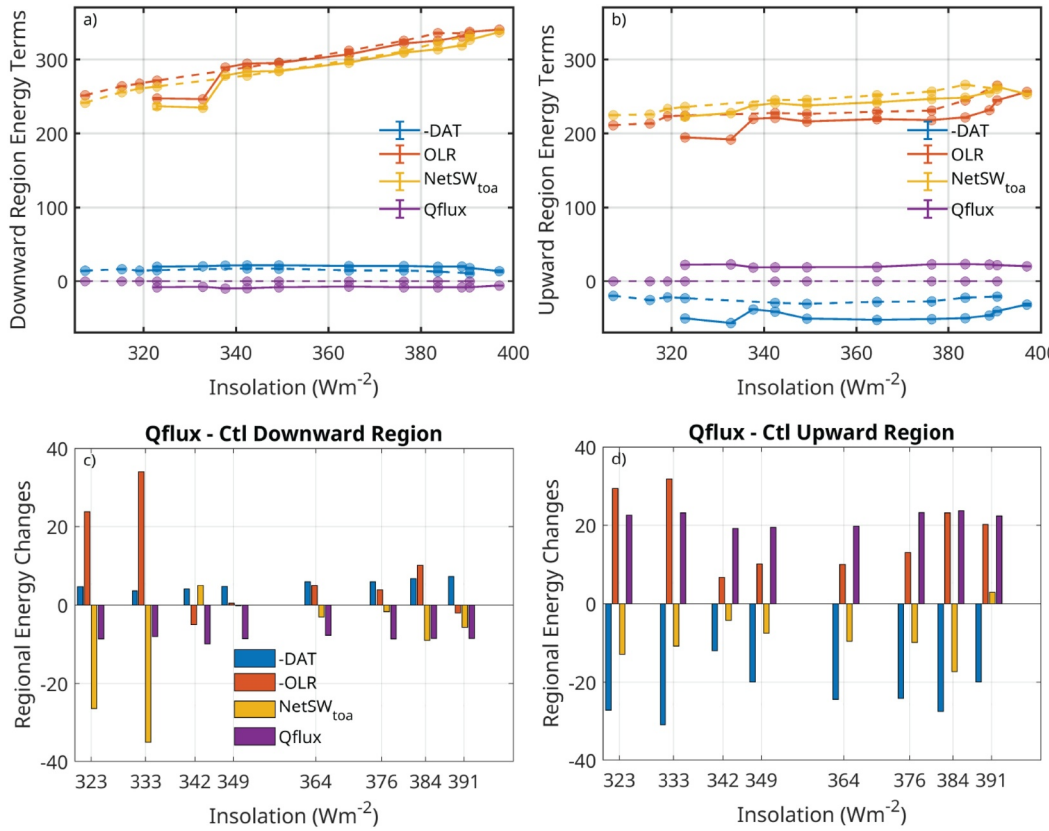

Figure 4. The top panels show regional energy terms, divergence of atmospheric energy flux (blue), outgoing longwave radiation (red), net shortwave at the top of the atmosphere (yellow), surface heat flux (purple) averaged over the region of ascending motion in panel (a) and the region of descending motion in panel (b). Dashed lines represent the control cases, solid the Q-flux cases. The bottom row shows bar charts of the same downward (c) and upward (d) regional energy variables, but instead show the change when adding Q-flux in experiments sharing the same insolation.

the descending region decreased absorbed solar energy is balanced primarily by decreased loss of OLR while the cooling due to Q-flux and the heating due to increased atmospheric energy convergence are smaller contributors. For the other, warmer cases in the subsiding region the energy budget responses to Q-flux are much smaller and the Q-flux is balanced in a variety of ways. Figure 4d shows that in the rising region the addition of heat by the Q-flux is offset predominantly by increased divergence of atmospheric transport (DAT). The bar charts for the warmest cases with 391 Wm^{-2} of insolation do not balance well. This is likely because the control case has a small SST contrast that oscillates chaotically so that the energy balances are less meaningful.

Comparing the temperature changes in Figure 3a with the energy budget changes in Figure 4a, we see that for the warmer cases with mean SST greater than about 300 K, the change in cold region temperature in response to Q-flux is significant, while the OLR changes in the cold region are rather small. This is possible because at tropical temperatures most of the OLR comes from the atmosphere, rather than the surface. Because there is no rotation, the atmosphere temperature profile above the boundary layer in the subsiding region is similar to the atmosphere temperature profile in the rising region. Because the warm region SST does not change much in response to Q-flux, the atmospheric temperature does not change much above the boundary layer, and the OLR therefore does not change much in response to Q-flux. In the downward region then, the surface temperature can decline without much reduction in OLR to suppress the cooling. In the region of rising motion, heat that is added by Q-flux is exported to the subsiding region, where it balances the OLR loss, which stays about the same despite the cooler surface with Q-flux. These mechanisms are similar to the ones that cause the intermediate climates to have a low sensitivity, as discussed in Hartmann and Dygert (2022).

To summarize, for the coldest climates with resulting global mean temperatures around 285 K, Q-flux produces a transition to a cold, high-SST-contrast state. An abrupt transition occurs across which the global mean SST

increases and the SST contrast decreases. In this warmer regime (300–309 K), Q-flux produces a global cooling, mostly associated with cooling in the subsiding region. This surface cooling in the subsiding region has only a small impact on the OLR in the subsiding region for the warmer cases because the atmospheric temperature is controlled by the warmest SST values, which do not change much in response to Q-flux.

3.3. Dynamic and Thermodynamic Responses to Q-Flux

To better understand how Q-flux affects the SST it is helpful to visualize how the circulation and thermodynamic properties respond to the addition of Q-flux. We will compare cases C349 and Q349 that have insolation of 349 Wm^{-2}, but with the latter having an added oceanic heat transport represented by a Q-flux. To show the structure compactly we plot circulation, relative humidity (RH) and air temperature as functions of pressure and SST area fraction. We divide the SST into 0.25 K intervals and then compute the area-averaged atmospheric structure for those SST bins. Each monthly grid cell from 40 years of simulation is identified by its SST, and variables of interest are averaged for each SST bin. Each SST bin also has a value that determines what fraction of the total area of the globe falls within the SST bin, $f_A(\mathrm{SST})$. The cumulative area fraction is computed by integrating this pdf of area fraction across SST, thus defining the cumulative "SST area fraction," which varies between zero and one.

$$\Phi_A(\mathrm{SST}) = \int_0^{\mathrm{SST}} f_A(\mathrm{SST})\, d\mathrm{SST} \tag{4}$$

A streamfunction can be computed by integrating the omega vertical velocity in Pa/s through area,

$$\Psi(\Phi_A, p) = \frac{A_E}{g} \int_0^{\Phi_A} \omega(p)\, d\Phi'_A \tag{5}$$

Here, A_E is the surface area of Earth, g is the acceleration of gravity and $\Psi(\Phi_A, p)$ has units of kgs^{-1}. The horizontal area velocity in m^2s^{-1} flowing toward the region of warm SST is then computed from,

$$V = -g\, \frac{d\Psi}{dp} \tag{6}$$

and the pressure velocity can be obtained from

$$\omega = \frac{g}{A_E}\, \frac{d\Psi}{d\Phi_A} \tag{7}$$

Figure 5 shows cross-sections in pressure versus SST area fraction coordinates for case C349 and its corresponding Q-flux case Q349 with the same insolation, 349 Wm^{-2}. Changes in the circulation with added Q-flux are illustrated through the streamfunction in panels a and b. With added Q-flux, the circulation strengthens and leads to more distinct shallow and deep cells. This helps to dry the troposphere over the coldest SSTs, as shown through RH in Figures 5c and 5d. The Q-flux case has a sharper vertical gradient of RH and a much larger area of very dry air above the boundary layer, consistent with the increase in subsidence drying. Figures 5e and 5f show the cross-sections of temperature. Although the coldest SSTs cool in response to Q-flux, air temperatures above the boundary layer are set by the warm pool and cool much less than the surface. So, while the surface temperature decreases in the subsiding region, the levels above the boundary layer where most of the OLR originates remain at about the same temperature after Q-flux is added. In addition, decreased emission from the surface through the atmospheric window region can be offset by the drier atmosphere above causing the atmospheric emission to move to slightly lower and warmer regions of the atmosphere.

In summary, we see the increase in circulation drying out the troposphere while the tropospheric air temperatures change only slightly above the boundary layer. This explains why, for the intermediate climates (300–309 K) the OLR in the subsiding region does not decrease much as the surface temperature is reduced by the addition of Q-flux.

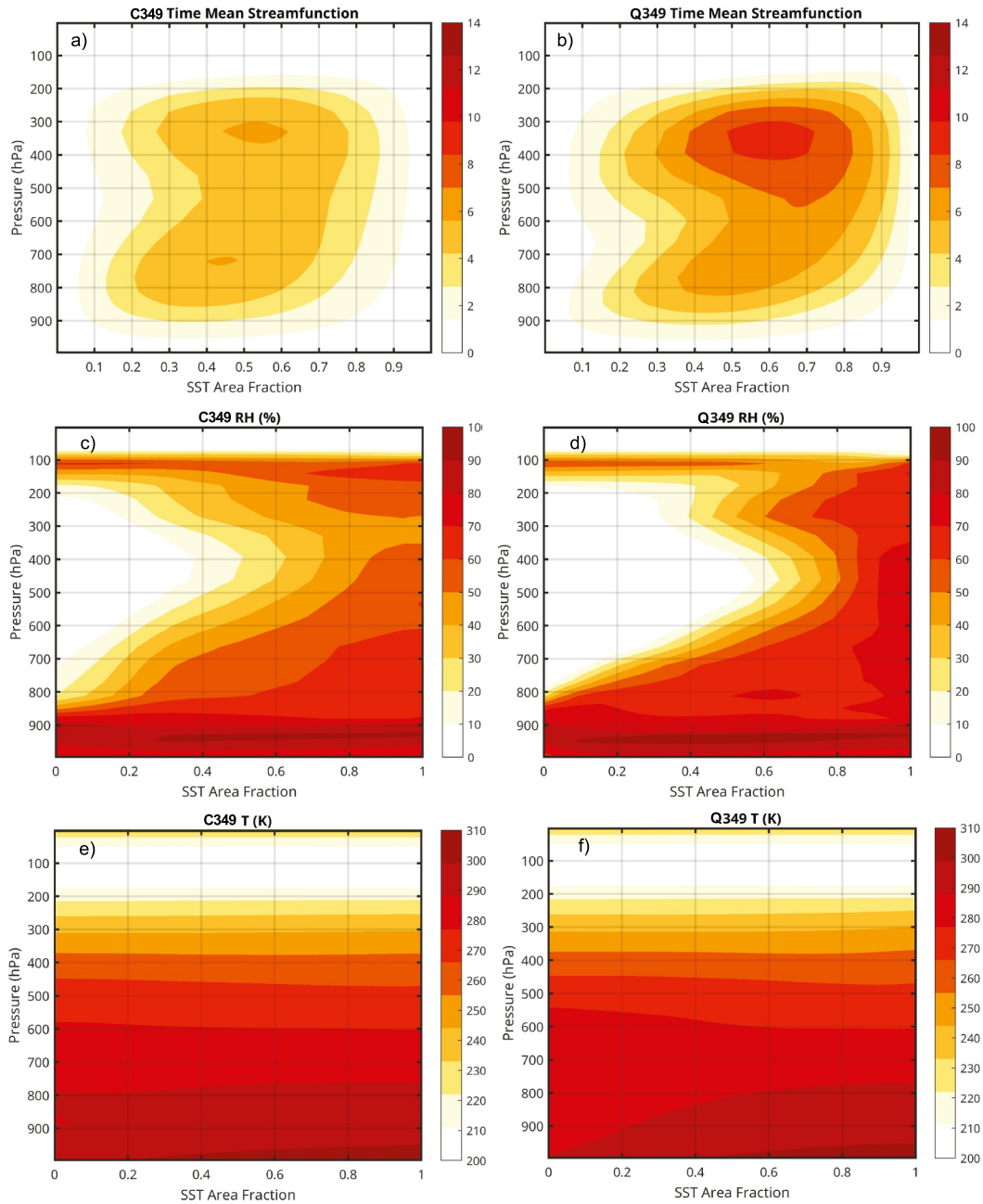

Figure 5. Comparisons of the vertical profiles in pressure coordinates, binned by Sea Surface Temperature area fraction between control case C349 and its Q-flux counterpart with the same insolation Q349. The top row shows the streamfunction $\left(1.0 \times 10^{11}\ \mathrm{kgs}^{-1}\right)$ strengthening, the second row shows the relative humidity (%) drying over the colder SSTs, and the third row shows the small temperature (K) changes in the mid troposphere where most of the outgoing longwave radiation originates.

3.4. The Greenhouse Effect and OLR Efficiency

To quantify the effect of atmospheric temperature and humidity structure on OLR, it is helpful to consider the greenhouse effect, GHE.

$$\mathrm{GHE} = \sigma T_s^4 - \mathrm{OLR} = \sigma T_s^4 (1 - E) \tag{8}$$

where E is the OLR efficiency defined by

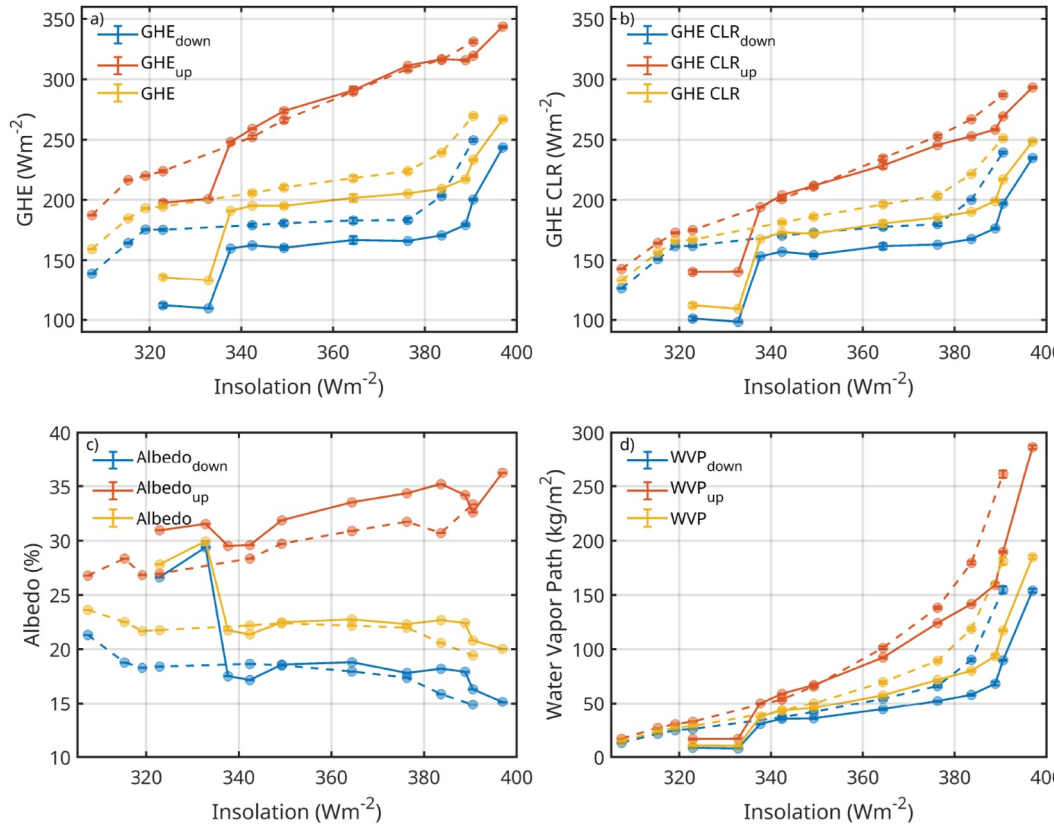

Figure 6. The top panels show the total (a) and clear-sky (b) greenhouse effect (GHE) in Wm^{-2} averaged over the region of ascending motion (orange), descending motion (blue) and globally (yellow). Panel (c) shows the albedo (%), and panel (d) shows the water vapor path in kgm^{-2}. The dashed lines represent the control cases and the solid lines represent the Q-flux cases.

$$E = \mathrm{OLR}/\sigma T_s^4 \tag{9}$$

We introduce E here so we can use the term "OLR efficiency" with a specific meaning. It is also a useful metric for the longwave effect of SST contrast on climate. We will see that Q-flux increases the OLR efficiency and that this is a primary mechanism whereby Q-flux cools the climate.

Figure 6 shows key variables for understanding the change in regional energy balance in response to Q-flux and insolation increases. Figure 6a shows the greenhouse effect as a function of insolation for the control and Q-flux cases. For the coldest cases, Q-flux causes a large decreases in the GHE because of the cooler surface and drier atmosphere. For the intermediate (300–309 K) cases, the addition of Q-flux reduces the greenhouse effect in the subsiding region by about 20 Wm^{-2}. Except for the two coldest cases, Q-flux has very little effect on the greenhouse effect in the upward region. Figure 6b shows that most of this changed GHE is present in the clear-sky fluxes and so does not depend on cloud changes. At the warmest temperatures greater than 310 K, the GHE over the subsiding region begins to increase, which is related to the rapid increase in water vapor path (WVP) in the subsiding region that is shown in Figure 6d. Figure 6c shows a large change in albedo between the coldest cases and the warmer cases, but in the intermediate regime where the mean SST is about 300–309 K the albedo in the downward region is insensitive to Q-flux and also does not change much as the mean SST warms from 300 to 309 K. The albedo in the upward region does increase somewhat in response to Q-flux, possibly because the increased SST gradient associated with Q-flux confines the deep convection and upward motion to a smaller part of the domain.

Figure 7 shows the OLR efficiency as defined in Equation 9 averaged over the upward, downward, and global domains for both the control and Q-flux experiments. For the global mean and downward regions, the OLR

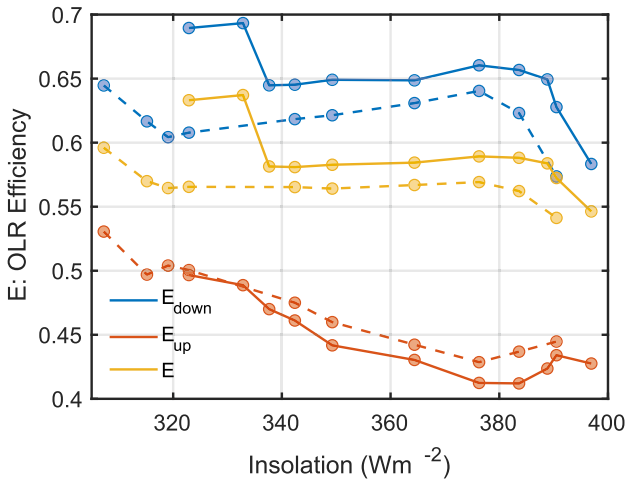

Figure 7. Outgoing longwave radiation efficiency E as in Equation 9, plotted versus insolation for the upward, downward and global domains for both the control (dashed line) and the Q-flux (solid line) experiments.

efficiency is greater in the Q-flux cases. This is because Q-flux lowers the SST in the subsiding region and also creates larger and drier subsiding zone. In the upward region, Q-flux actually reduces the OLR efficiency by concentrating the convection in a smaller area. For the two coldest cases in the Q-flux experiment, the OLR efficiency is very high and contributes significantly to the cooling in those cases. At the warmest temperatures, the OLR efficiency declines as the SST contrast declines and explains much of the greater sensitivity of the warmest climates. Most of this reduced OLR efficiency at high temperatures is produced in the subsiding region, where the WVP is increasing (Figure 6d).

To summarize, focusing on the intermediate climates with SST between 300 and 309 K, we see that the primary mechanism whereby Q-flux cools the mean climate is by increasing the OLR efficiency, the amount of OLR generated for a given mean SST value. OLR efficiency can be increased three ways: (a) by increasing the SST contrast between dry subsiding regions and warm convective regions, (b) by increased drying of the troposphere in the subsiding region, further decreasing the greenhouse effect, and (c) by increasing the SF, as regions of downward motion have drier tropospheres, and the smaller greenhouse effect leads to more efficient OLR. Since the free troposphere temperature is similar everywhere in the tropics, the air temperature is determined by convection occurring over the warmest water. Since at tropical temperatures most of the OLR comes from the atmosphere, by increasing the SST contrast the mean surface temperature can be decreased while the OLR changes relatively little. The longwave emission from the atmosphere is largely determined by the temperature at the emission level and the water vapor above that (Hartmann et al., 2022; Jeevanjee & Fueglistaler, 2020). The OLR efficiency in the cold subsiding region is affected by the RH and temperature of the free atmosphere above but also by the coldness of the surface and boundary layer temperatures. For fixed boundary layer RH, cooling the surface increases the longwave efficiency because the cooler boundary layer contains less water vapor.

3.5. Cloud Response

In Figure 4, we saw that the changes of OLR and absorbed shortwave in response to the addition of Q-flux are much larger for the cold regime (<300 K), but much smaller for the intermediate and warm (>309 K) regimes. The large changes in the cold regime are driven by low cloud changes. In this section, we look at the cloud contribution to the changes in reflected short-wave radiation.

Figure 8 shows several variables, averaged over the coldest 20% of SSTs, a useful focus for understanding the change in clouds in the cold regime. Figure 8a shows the albedo and low cloud fraction. In the cold regime, Q-flux causes a drastic increase in both albedo and low cloud fraction. As shown in Figure 8b, this translates to a large increase in shortwave cloud radiative effect (SWCRE), and a small changes in longwave cloud radiative effect (LWCRE). The increase in low clouds corresponds to a large increase in inversion strength compared to the case without Q-flux, as shown in Figure 8 panel c. Figure 8 panel c shows both the estimated inversion strength (EIS) (Wood & Bretherton, 2006), and the lower troposphere stability (Klein & Hartmann, 1993). Figure 8 panel d shows the WVP scaled by 1,000 and liquid water path (LWP). The WVP is particularly low for the cold regime while the LWP is enhanced there. As the insolation is increased and the climate warms, the WVP above the boundary layer increases, which increases downwelling longwave radiation that could suppress the low clouds (Bretherton & Khairoutdinov, 2015; Eastman & Wood, 2018; Schneider et al., 2019).

To summarize, in the cold regime Q-flux induces a large increase in low clouds that correlates with an increase in inversion strength and a large decrease in temperature. Low temperature and high inversion strength both favor low cloud abundance through thermodynamic and dynamic mechanisms (Bretherton & Blossey, 2014; Bretherton & Khairoutdinov, 2015). The transition from the cold regime to the intermediate regime is marked by a large decrease in low clouds corresponding to decreasing EIS, warmer SST and an increase in WVP above the boundary layer. These responses are all in accord with our general understanding of low clouds in the atmosphere.

In the intermediate regime, the change in low clouds from the control experiments to the Q-flux experiments is small due to three main competing effects: (a) for the same insolation, the subsiding region is colder in the case with

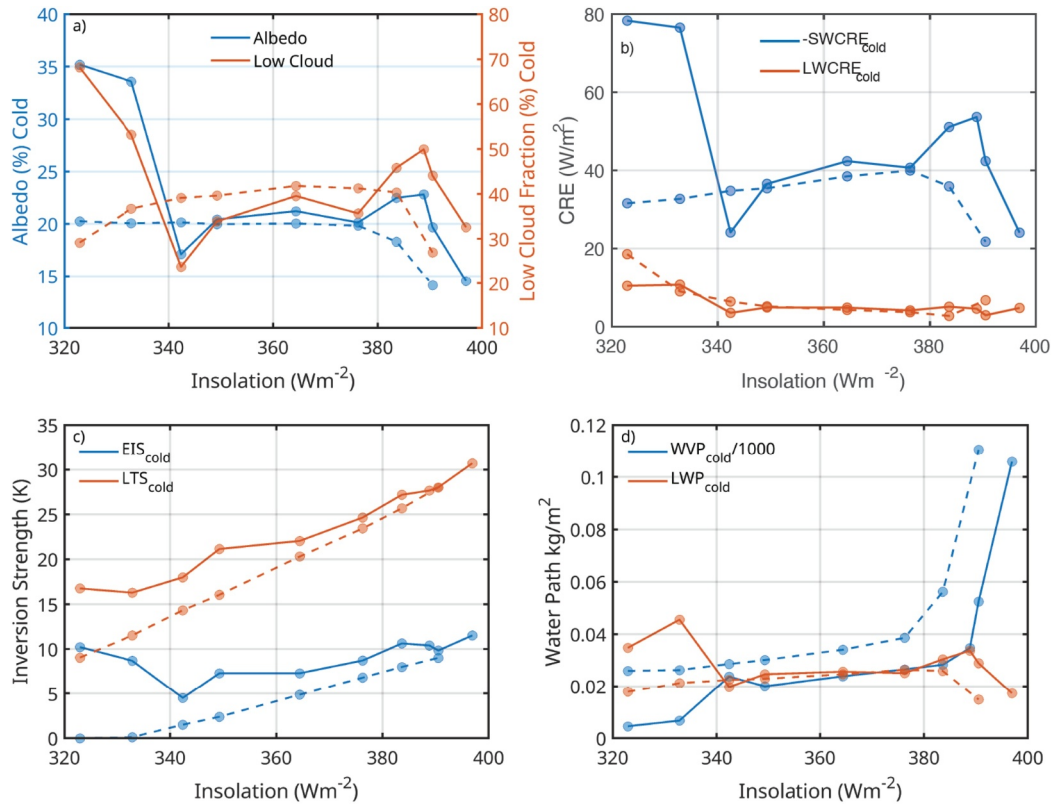

Figure 8. Key cloud variables averaged over coldest 20% Sea Surface Temperatures (SSTs): (a) albedo and low cloud fraction (%), (b) negative shortwave (-SWCRE) and longwave (LWCRE) cloud radiative effect, (c) estimated inversion strength and lower troposphere stability, and (d) water vapor path (WVP/1,000) divided by 1,000 for scaling and liquid water path in kgm^{-2}. Note that SWCRE is plotted with reversed sign for clarity. Dashed line indicate the control case and solid lines indicate the Q-flux case.

Q-flux, and this favors more low clouds, (b) the Q-flux increases the SST contrast, which leads to a stronger inversion above the boundary layer, which if acting alone would lead to an increase in low clouds, and (c) the Q-flux leads to a drier troposphere, which increases entrainment drying, which would decrease the low clouds if acting alone (Bretherton & Blossey, 2014). For warmer temperatures (>300 K), entrainment drying plays a larger role than in the cold regime, and the low clouds respond only weakly to Q-flux.

Finally, for the very warm temperatures (>309 K), the low cloud fractions and albedo decrease dramatically as the SST contrast also declines. Associated with this breakdown of the SST contrast is a rapid increase in the WVP over the colder water (Figure 8d), which decreases the longwave cooling of the boundary layer clouds in the subsiding region. This rapid increase in WVP occurs at a higher insolation for the case with Q-flux because the Q-flux cases are colder than the control cases. Thus, at the 310 K transition, although the inversion strength remains, both the increased temperature and the reduced longwave cooling of the boundary layer act to reduce the low cloud abundance in the cold region.

The transition from the cold regime to the intermediate regime is dominated by the reduction in low clouds over the subsiding region and is therefore likely to be sensitive to the low cloud parameterization in the model. The transition, however, appears physically reasonable and consistent with previous studies. Specifically, Schneider et al. (2019) found a similar, drastic decline in stratiform clouds with warming using large eddy simulations. There are several potential factors contributing to the decline in low clouds (Bretherton & Blossey, 2014). Schneider et al. (2019) highlight the importance of cloud top radiative cooling for generating the turbulence responsible for maintaining stratiform clouds. Eastman and Wood (2018) use observational data to address the competing influences of increasing inversion strength with changes in specific humidity: including, (a) stability, (b) the specific humidity just above the boundary layer, and (c) the column humidity in the free troposphere. The specific humidity immediately above the boundary layer impacts the efficiency of entrainment drying while the

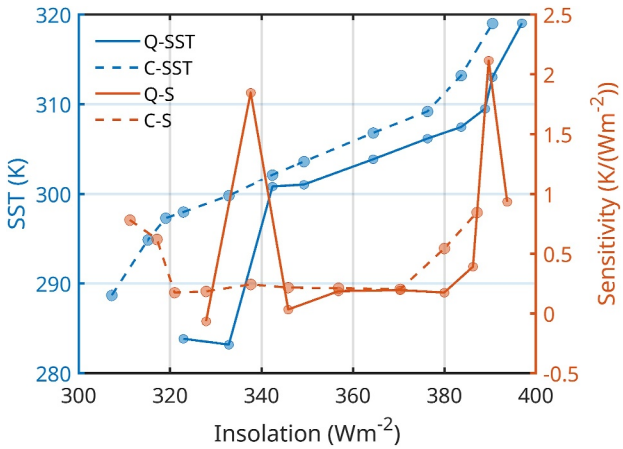

Figure 9. The blue lines show the global mean Sea Surface Temperature (SST) (K) versus insolation $\left(\mathrm{Wm}^{-2}\right)$, with the dashed lines representing the control cases and the solid lines representing cases with the Q-flux added. The orange lines represent the slope of the blue lines, or the change in SST per change in insolation $\left(\mathrm{K/Wm}^{-2}\right)$.

total column humidity impacts the downwelling longwave radiation at the boundary layer top. While increasing the inversion strength would lead to an increase in low clouds, increasing the specific humidity gradient leads to enhanced entrainment drying and a decrease in low clouds (Bretherton & Blossey, 2014; Wood & Bretherton, 2006). Cloud top radiative cooling and entrainment drying impact albedo through stratocumulus thinning and cloud lifetime respectively (Eastman & Wood, 2018).

Although the clouds do contribute to the overall cooling with Q-flux, apart from the cold regime (<300 K) the cloud change is small in comparison to other energy budget variables such as energy transport out of the warm region and increased efficiency of OLR in the cold region. If the clouds were responsible for the cooling, we would expect to see a large decrease in net shortwave radiation and a decrease in OLR of the same magnitude as the SST decreases. Instead, we see only a small decrease in OLR and net shortwave radiation. So, although the clouds do cool more in Q-flux cases, with the most change occurring in the hottest cases, they are not the main mechanism responsible for the decrease in global mean SST in response to Q-flux, except in cold cases before the transition from the cold regime to the intermediate regime.

3.6. Sensitivity to Forcing

Adding the Q-flux results in a decrease in global mean SST when compared with the control simulation with the same forcing. One might ask if this cooling has any effect on the sensitivity of the climate to forcing. We are changing insolation rather than carbon dioxide levels to vary the climate. Here, we will define our sensitivity to forcing as

$$S = \frac{\Delta \mathrm{SST}}{\Delta I} \tag{10}$$

where ΔSST is the change in global mean SST and ΔI is the change in insolation. This definition is not consistent with the way global sensitivity is calculated, since the insolation change is not the forcing change. Some fraction of the insolation is reflected, so that the forcing is smaller than the change in insolation. We seek here not to provide a precise estimate of sensitivity, but merely to show that significant changes in sensitivity occur at the regime transitions in our experiments.

Figure 9 shows the sensitivity defined by Equation 10 for the cases with and without the Q-flux. For the cases with intermediate global mean SSTs (300–309 K), the implied sensitivities of the control and the Q-flux cases are similar. While Q-flux cools the climate in comparison to the control case, it does not result in substantially different sensitivity to insolation increases for most values of insolation. Exceptions to this occur at the transition from the cool to the intermediate regime, and when moving to the warmest cases. For the warm transition near 310 K, the Q-flux cases make a much more rapid transition and at higher insolation values, although similar temperatures. Both the control cases and the Q-flux cases see a sudden change in sensitivity after reaching 310 K. This shift is attributed to the increase in water vapor that causes the subsiding region to become less efficient at cooling to space (Figure 8d).

While the different regimes affect the global mean SST, they do not affect the overall change in sensitivity within regimes when comparing the Q-flux cases to those without. Instead, at each regime transition, there is a large spike in sensitivity as an SST cooling mechanism is lost. Moving from the cold regime where the clouds dominate to a climate where greenhouse effect dominates, there is a sudden decrease in cloud fraction that results in a large global mean SST increase associated with a decrease in the SST contrast. The cooling response to Q-flux in the intermediate regime comes from the increased OLR efficiency from the reduced greenhouse effect associated with the SST contrast. When the SST becomes warm enough that the greenhouse effect begins to grow in the subsiding region, the cooling associated with the SST contrast is lost and another spike in sensitivity occurs in the transition to warm climates where the radiator-fin cooling mechanism becomes less efficient.

The lack of change in sensitivity when comparing the cases with and without Q-flux is consistent with Zhang et al. (2020), which shows that despite large variations in SST distributions leading to large regional variations in local OLR feedbacks, the global-mean OLR sensitivity is nearly the same across a suite of climate models. They argue that this is due to linearity of clear-sky OLR on surface temperature for a fixed RH profile (Koll & Cronin, 2018), and relatively small changes in the RH distribution with warming. Our results are consistent with this interpretation to the extent that changes in RH in dry zones are offset by opposite changes in RH in wet zones, and air temperature is controlled by the warmest SST, which does not respond strongly to Q-Flux in our simulations. This interpretation is supported by Figure 7, which shows that the global mean OLR efficiency is near constant across a range of insolation values for both the control and Q-flux experiments, despite the mean difference between them showing greater efficiency in the Q-flux cases.

To summarize, although adding Q-flux results in cooler global mean SSTs compared with the corresponding control case, Q-flux does not result in large changes to the implied climate sensitivity, except at the transitions between the cold and intermediate, and the intermediate and warm regimes. Adding Q-flux delays the onset of the high sensitivity associated with very warm climates until higher values of insolation, but the temperature threshold remains unchanged at about 310 K.

4. Comparison to ENSO Observations

In this section, we will use ERA5 reanalysis data to compare behaviors of the model with nature. The most likely real-world analog for these experiments is the ENSO in which the east-west gradient of ocean heat transport varies from a small gradient in El Niño years, similar to our control experiments, and a large gradient in La Niña years (Figure 1), similar to our Q-flux experiments. We use monthly average, one degree horizontal resolution data from ERA5 (Hersbach et al., 2020) from 1990 to 2020. The variables used are the surface energy budget terms, top of the atmosphere energy, and SST. We use the vertically integrated divergence of energy transport (DAT) from a mass-consistent data set (Mayer et al., 2021).

We again use the Niño 3.4 index to represent the phase of ENSO, with positive values indicating an El Niño phase and negative values indicating a La Niña phase. We use reanalysis data averaged from 10S to 10N over tropical oceans to get a sense for how key variables vary zonally and how that changes between ENSO phases. Figure 10 shows top of the atmosphere energy variables and the SST binned by standard deviations of the Niño 3.4 index and longitude. Note that for the energy budget terms, the color scale is arranged so that the changes can be directly compared. This shows in particular the larger changes in atmospheric energy divergence compared with the longwave and shortwave terms. In the Q-flux experiments, we saw that the hottest SSTs did not increase as much as the coldest SSTs cooled. We see a similar phenomenon in the reanalysis data, as shown in Figure 10a. Increased upwelling cools the coldest SSTs, but there is a much smaller decrease in the hottest SSTs. To better understand what is affecting the change in SSTs, we look at the top of the atmosphere energy budget terms.

The energy budget terms also show similar variations as our idealized experiments. Figure 10b, shows that OLR decreases only modestly in the La Niña phase, compared with the DAT changes. In Figure 10d, the net shortwave at the top of the atmosphere shows only small changes over the coldest SSTs, again compared to DAT changes. Over intermediate and warm SSTs, OLR and SWnet show individual changes on the order of 20 Wm^{-2} in which the longwave and shortwave effects offset each other. Among the energy budget terms, DAT, shown in Figure 10c, sees the largest change between La Niña and El Niño phases in the Eastern Pacific. There is an increase in convergence of atmospheric energy flux over the coldest SSTs in the La Niña phase and an increase in export from the warmer SSTs. This is consistent with the increased SST gradient leading to a stronger circulation and increased atmospheric transport.

Despite the larger changes in SST in the cold region, the OLR and SWnet in this region change modestly compared to the changes in DAT. The warmest SSTs appear to be constrained by an increase in energy export out of the region in both cases.

Significant differences exist between our idealized modeling results and the ENSO cycle represented in the reanalysis data. In our modeling experiments, insolation is uniform and there is no systematic energy transport from the tropics toward the poles. In nature, there is a systematic atmospheric energy transport out of the tropics to the mid latitudes. In nature, much of the subsidence occurs in the subtropics under the Hadley Cells and in the presence of rotation.

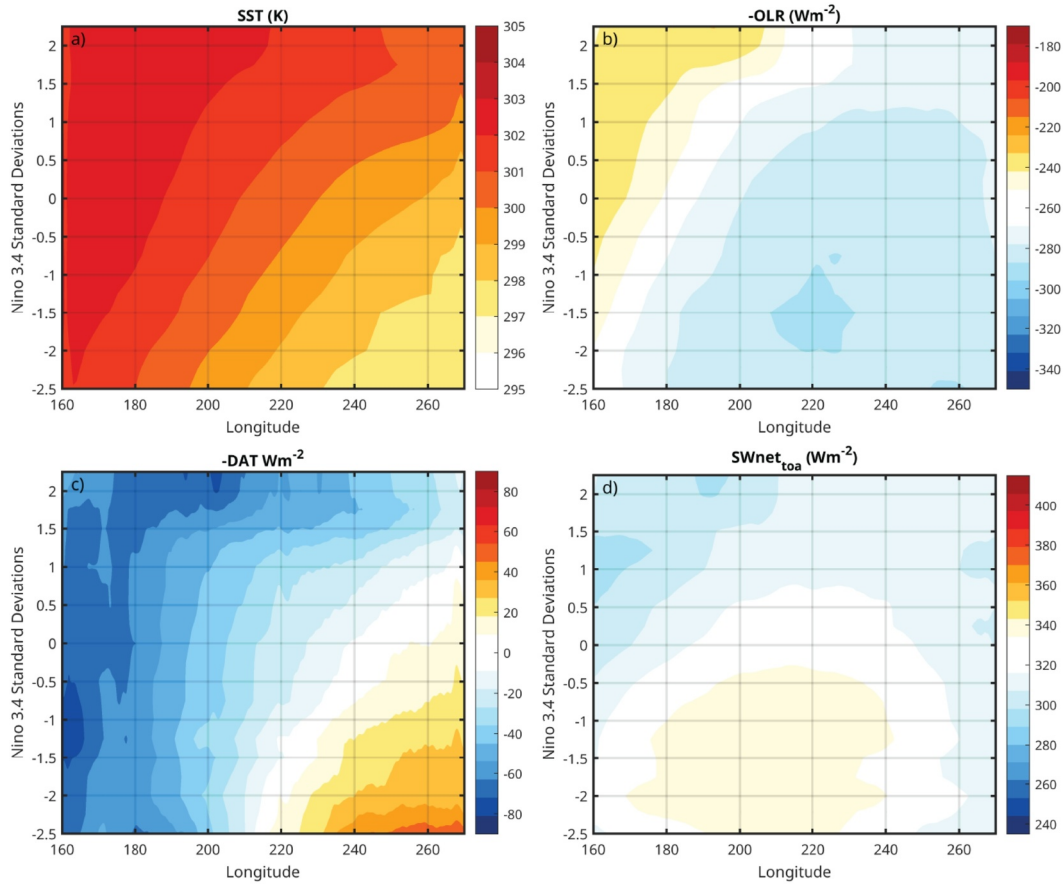

Figure 10. Panel (a) shows the Sea Surface Temperature (K) binned by Niño 3.4 standard deviations and longitude, with 0.25 K contour intervals. Panels (b)–(c) show top of the atmosphere energy budget terms (b) outgoing longwave radiation, (c) DAT, and (d) NetSW with 10 Wm^{-2} contour intervals. Data over land are removed so that we use the meridional mean over tropical waters from −10° S to 10° N.

5. Summary

Ocean heat transport in the form of Q-flux has been added to a global radiative equilibrium model of an atmosphere above a slab ocean. The global mean temperature is reduced by the addition of Q-flux. Adding Q-flux leads to stronger SST contrast by cooling the coldest SSTs, which leads to stronger circulation and stronger winds. Stronger winds also help the warmest SSTs stay approximately unchanged despite the added heat in the warm region. The warm region is prevented from warming in response to Q-flux by increased export of energy from the region of upward motion over the warmest SSTs. While the atmosphere exports more heat from the warm pool, the large-scale circulation warms and dries the upper troposphere in the subsiding region. This contrast produced by Q-flux increases the OLR achieved for a particular mean SST, which produces a cooler planet for the same insolation value, even in the absence of cloud effects.

The response of the model to adding Q-flux depends on the regime of global mean SST. For relatively cold mean SST, Q-flux causes a transition to a very cold, high-SST-contrast state. Increased low clouds in the cold region are the main factor in cooling the global mean SST and increasing its contrast in these cold states. As the insolation is increased from these cold cases, an abrupt transition occurs where the low cloud reflectivity decreases, the SST contrast decreases and the mean SST increases. Above this cold transition mean SST values are near those of the current tropics, and cloud changes play a small role as the insolation is further increased.

A second transition occurs near mean SST values of 310 K. At this point, the SST contrast declines and the climate becomes much more sensitive to further increases in insolation. Because it cools the mean climate, Q-flux delays this transition to a warm and sensitive climate to higher values of insolation, but again the transition is more

abrupt than in the case without Q-flux. Oceanic heat transport results in stronger convective organization, promoting both the increase in low clouds seen in the coldest case and the reduction in the greenhouse effect over the subsiding region for the intermediate cases most like the current tropics.

Despite the large changes in circulation from the control to the Q-flux experiments, for cases with mean SST similar to the current tropics (300–309 K) there are only small changes in cloud fraction and albedo as the climate is warmed. The role of clouds is probably strongly model dependent, and cloud feedbacks could play a more significant role in a different model. Our main conclusions, however, can be shown through clear-sky values alone, which are more robust across different models.

Major caveats regarding these results are that the parameterizations affecting the low cloud amount in the simulations are uncertain and likely important to the regime behavior of the model. Also, the fixed position of the convective region and the lack of meteorology driven by rotation likely result in a subsiding region that is drier than found in nature. It is nonetheless true that the SST contrast is as important to the radiator fin mechanism as the RH contrast because of the strong dependence of boundary layer humidity on temperature.

To summarize, we have shown that

- Adding a Q-flux that mimics ocean heat transport cools the global mean SST by cooling the coldest SSTs.
- Although ocean heat transport provides heating under the warmest SSTs, the warmest SSTs do not increase much compared to the control case without Q-flux.
- Although the warm, ascending region sees changes in both longwave and shortwave radiative effects, the net radiation change is small; instead, the atmospheric energy transport out of the ascending region increases to balance the convergence of Q-flux.
- For cases most like the current tropics, the OLR over the coldest SSTs only decreases a small amount despite the large decrease in SST because the air temperature is tied to the warmest SSTs, and increased circulation leads to a drier mid troposphere in the subsiding region, which decreases the greenhouse effect and allows for more efficient longwave cooling to space.
- Although the Q-flux cools the global mean SST, it does not affect the climate sensitivity of the model. It does, however, delay the transition between SST regimes, particularly the onset of the higher sensitivity warm climates.
- Observations of ENSO events show a similar breakdown of the most important terms as in our Q-flux experiments.

Data Availability Statement

The model used is Geophysical Fluid Dynamics Laboratory's (GFDL) AM2.1 (Anderson et al., 2004). Data and code supporting figures are available through Zenodo (Dygert & Hartmann, 2025). Most ERA5 variables are downloaded from the main database (Copernicus Climate Change Service, 2022), and only the DAT is from a mass consistent dataset (Mayer et al., 2021).

Acknowledgments
The three reviewers of this paper provided perceptive and important insights and suggestions that greatly improved the quality and readability of this work. This work was supported by NSF Grant AGS-2124496, and the code for AM2.1 was provided by the NOAA Geophysical Fluid Dynamics Laboratory.

References

Anderson, J. L., Balaji, V., Broccoli, A. J., Cooke, W. F., Delworth, T. L., Dixon, K. W., et al. (2004). The new GFDL global atmosphere and land model AM2-LM2: Evaluation with prescribed SST simulations. *Journal of Climate*, *17*(24), 4641–4673.

Andrews, T., Gregory, J. M., Paynter, D., Silvers, L. G., Zhou, C., Mauritsen, T., et al. (2018). Accounting for changing temperature patterns increases historical estimates of climate sensitivity. *Geophysical Research Letters*, *45*(16), 8490–8499. https://doi.org/10.1029/2018GL078887

Armour, K. C. (2017). Energy budget constraints on climate sensitivity in light of inconstant climate feedbacks. *Nature Climate Change*, *7*(5), 331–335. https://doi.org/10.1038/nclimate3278

Armour, K. C., Proistosescu, C., Dong, Y., Hahn, L. C., Blanchard-Wrigglesworth, E., Pauling, A. G., et al. (2024). Sea-surface temperature pattern effects have slowed global warming and biased warming-based constraints on climate sensitivity. *Proceedings of the National Academy of Sciences*, *121*(12), e2312093121. https://doi.org/10.1073/pnas.2312093121

Bjerknes, J. (1966). A possible response of the atmospheric Hadley circulation to equatorial anomalies of ocean temperature. *Tellus*, *18A*(4), 820–829. https://doi.org/10.3402/tellusa.v18i4.9712

Bretherton, C. S., & Blossey, P. N. (2014). Low cloud reduction in a greenhouse-warmed climate: Results from Lagrangian LES of a subtropical marine cloudiness transition. *Journal of Advances in Modeling Earth Systems*, *6*(1), 91–114. https://doi.org/10.1002/2013MS000250

Bretherton, C. S., Blossey, P. N., & Khairoutdinov, M. (2005). An energy-balance analysis of deep convective self-aggregation above uniform SST. *Journal of the Atmospheric Sciences*, *62*(12), 4273–4292. https://doi.org/10.1175/JAS3614.1

Bretherton, C. S., & Khairoutdinov, M. F. (2015). Convective self-aggregation feedbacks in near-global cloud-resolving simulations of an aquaplanet. *Journal of Advances in Modeling Earth Systems*, *7*(4), 1765–1787. https://doi.org/10.1002/2015MS000499

Cheng, L., Trenberth, K. E., Fasullo, J. T., Mayer, M., Balmaseda, M., & Zhu, J. (2019). Evolution of ocean heat content related to ENSO. *Journal of Climate*, *32*(12), 3529–3556. https://doi.org/10.1175/JCLI-D-18-0607.1

Copernicus Climate Change Service. (2022). Mass-consistent atmospheric energy and moisture budget monthly data from 1979 to present derived from ERA5 reanalysis. *ECMWF*. https://doi.org/10.24381/CDS.C2451F6B

Coppin, D., & Bony, S. (2015). Physical mechanisms controlling the initiation of convective self-aggregation in a general circulation model. *Journal of Advances in Modeling Earth Systems*, *7*(4), 2060–2078. https://doi.org/10.1002/2015MS000571

Coppin, D., & Bony, S. (2017). Internal variability in a coupled general circulation model in radiative-convective equilibrium. *Geophysical Research Letters*, *44*(10), 5142–5149. https://doi.org/10.1002/2017GL073658

Coppin, D., & Bony, S. (2018). On the interplay between convective aggregation, surface temperature gradients, and climate sensitivity. *Journal of Advances in Modeling Earth Systems*, *10*(12), 3123–3138. https://doi.org/10.1029/2018MS001406

Cronin, T. W., & Wing, A. A. (2017). Clouds, circulation, and climate sensitivity in a radiative-convective equilibrium channel model. *Journal of Advances in Modeling Earth Systems*, *9*(8), 2883–2905. https://doi.org/10.1002/2017MS001111

Dong, Y., Armour, K. C., Zelinka, M. D., Proistosescu, C., Battisti, D. S., Zhou, C., & Andrews, T. (2020). Intermodel spread in the pattern effect and its contribution to climate sensitivity in CMIP5 and CMIP6 models. *Journal of Climate*, *33*(18), 7755–7775. https://doi.org/10.1175/JCLI-D-19-1011.1

Dong, Y., Proistosescu, C., Armour, K. C., & Battisti, D. S. (2019). Attributing historical and future evolution of radiative feedbacks to regional warming patterns using a green's function approach: The preeminence of the Western Pacific. *Journal of Climate*, *32*(17), 5471–5491. https://doi.org/10.1175/JCLI-D-18-0843.1

Dygert, B. D., & Hartmann, D. L. (2023). The cycle of large-scale aggregation in tropical radiative-convective equilibrium. *Journal of Geophysical Research: Atmospheres*, *128*(7), e2022JD037302. https://doi.org/10.1029/2022JD037302

Dygert, B. D., & Hartmann, D. L. (2025). Effects of ocean heat transport in tropical radiative convective equilibrium [Dataset]. *model data*. https://doi.org/10.5281/zenodo.15238335

Eastman, R., & Wood, R. (2018). The competing effects of stability and humidity on subtropical stratocumulus entrainment and cloud evolution from a lagrangian perspective. *Journal of the Atmospheric Sciences*, *75*(8), 2563–2578. https://doi.org/10.1175/JAS-D-18-0030.1

Hartmann, D. L. (2016). *Global physical climatology* (2nd ed., p. 40). Elsevier.

Hartmann, D. L., & Dygert, B. D. (2022). Global radiative convective equilibrium with a slab Ocean: SST contrast, sensitivity and circulation. *Journal of Geophysical Research: Atmospheres*, *127*(12), e2021JD036400. https://doi.org/10.1029/2021JD036400

Hartmann, D. L., Dygert, B. D., Blossey, P. N., Fu, Q., & Sokol, A. B. (2022). The vertical profile of radiative cooling in radiative-convective equilibrium: Moist adiabat versus entrainment-modified plume model. *Journal of Climate*, *35*(19), 6253–6265. https://doi.org/10.1175/JCLI-D-21-0861.1

Held, I. M., Hemler, R. S., & Ramaswamy, V. (1993). Radiative-convective equilibrium with explicit two-dimensional moist convection. *Journal of the Atmospheric Sciences*, *50*(23), 3909–3927. (Geophys. Fluid Dynamics Lab., NOAA, Princeton Univ., NJ, USA). https://doi.org/10.1175/1520-0469(1993)050<3909:rcewet>2.0.co;2

Held, I. M., Zhao, M., & Wyman, B. (2007). Dynamic radiative–convective equilibria using GCM column physics. *Journal of the Atmospheric Sciences*, *64*(1), 228–238. https://doi.org/10.1175/JAS3825.11

Hersbach, H., Bell, B., Berrisford, P., Hirahara, S., Horányi, A., Muñoz-Sabater, J., et al. (2020). The ERA5 global reanalysis. *Quarterly Journal of the Royal Meteorological Society*, *146*(730), 1999–2049. https://doi.org/10.1002/qj.3803

Horel, J. D., & Wallace, J. M. (1981). Planetary-scale atmospheric phenomena associated with the southern oscillation. *Monthly Weather Review*, *109*, 813–829. https://doi.org/10.1175/1520-0493(1981)109⟨0813:PSAPAW⟩2.0.CO;2

Jeevanjee, N., & Fueglistaler, S. (2020). On the cooling-to-space approximation. *Journal of the Atmospheric Sciences*, *77*(2), 465–478. https://doi.org/10.1175/JAS-D-18-0352.1

Klein, S., & Hartmann, D. (1993). The seasonal cycle of low stratiform clouds. *Journal of Climate*, *6*(8), 1587–1606. https://doi.org/10.1175/1520-0442(1993)006<1587:tscols>2.0.co;2

Koll, D. D. B., & Cronin, T. W. (2018). Earth's outgoing longwave radiation linear due to H_2O greenhouse effect. *Proceedings of the National Academy of Sciences*, *115*(41), 10293–10298. https://doi.org/10.1073/pnas.1809868115

Larson, K., Hartmann, D. L., & Klein, S. A. (1999). The role of clouds, water vapor, circulation, and boundary layer structure in the sensitivity of the tropical climate. *Journal of Climate*, *12*(8), 2359–2374. (Using Smart Source Parsing pt.1; Aug). https://doi.org/10.1175/1520-0442(1999)012<2359:trocwv>2.0.co;2

Mayer, J., Mayer, M., & Haimberger, L. (2021). Mass-consistent atmospheric energy and moisture budget monthly data from 1979 to present derived from ERA5 reanalysis [Dataset]. https://doi.org/10.24381/cds.c2451f6b

Meraner, K., Mauritsen, T., & Voigt, A. (2013). Robust increase in equilibrium climate sensitivity under global warming. *Geophysical Research Letters*, *40*(22), 5944–5948. https://doi.org/10.1002/2013GL058118

Miller, R. (1997). Tropical thermostats and low cloud cover. *Journal of Climate*, *10*(3), 409–440. https://doi.org/10.1175/1520-0442(1997)010<0409:ttalcc>2.0.co;2

Pierrehumbert, R. T. (1995). Thermostats, radiator fins, and the local runaway greenhouse. *Journal of the Atmospheric Sciences*, *52*(10), 1784–1806. https://doi.org/10.1175/1520-0469(1995)052⟨1784:TRFATL⟩2.0.CO;2

Popke, D., Stevens, B., & Voigt, A. (2013). Climate and climate change in a radiative-convective equilibrium version of ECHAM6. *Journal of Advances in Modeling Earth Systems*, *5*(1), 1–14. https://doi.org/10.1029/2012MS000191

Reed, K. A., & Chavas, D. R. (2015). Uniformly rotating global radiative-convective equilibrium in the Community Atmosphere Model, version 5. *Journal of Advances in Modeling Earth Systems*, *7*(4), 1938–1955. https://doi.org/10.1002/2015MS000519

Retsch, M. H., Mauritsen, T., & Hohenegger, C. (2019). Climate change feedbacks in aquaplanet experiments with explicit and parametrized convection for horizontal resolutions of 2,525 up to 5 km. *Journal of Advances in Modeling Earth Systems*, *11*(7), 2070–2088. https://doi.org/10.1029/2019MS001677

Russell, G. L., Lacis, A. A., Rind, D. H., Colose, C., & Opstbaum, R. F. (2013). Fast atmosphere-ocean model runs with large changes in CO_2. *Geophysical Research Letters*, *40*(21), 5787–5792. https://doi.org/10.1002/2013GL056755

Schneider, T., Kaul, C. M., & Pressel, K. G. (2019). Possible climate transitions from breakup of stratocumulus decks under greenhouse warming. *Nature Geoscience*, *12*(3), 163–167. https://doi.org/10.1038/s41561-019-0310-1

Stevens, B., Sherwood, S. C., Bony, S., & Webb, M. J. (2016). Prospects for narrowing bounds on Earth's equilibrium climate sensitivity. *Earth's Future*, *4*(11), 512–522. https://doi.org/10.1002/2016EF000376

Tompkins, A. M. (2001). Organization of tropical convection in low vertical wind shears: The role of cold pools. *Journal of the Atmospheric Sciences*, *58*(13), 1650–1672. https://doi.org/10.1175/1520-0469(2001)058⟨1650:OOTCIL⟩2.0.CO;2

Wing, A. A., Emanuel, K., Holloway, C. E., & Muller, C. (2017). Convective self-aggregation in numerical simulations: A review. *Surveys in Geophysics*, *38*(6), 1173–1197. https://doi.org/10.1007/s10712-017-9408-4

Wood, R., & Bretherton, C. S. (2006). On the relationship between stratiform low cloud cover and lower-tropospheric stability. *Journal of Climate*, *19*(24), 6425–6432. https://doi.org/10.1175/JCLI3988.1

Zhang, Y., Jeevanjee, N., & Fueglistaler, S. (2020). Linearity of outgoing longwave radiation: From an atmospheric column to global climate models. *Geophysical Research Letters*, *47*(17), e2020GL089235. https://doi.org/10.1029/2020GL089235

Zhou, C., Zelinka, M. D., & Klein, S. A. (2016). Impact of decadal cloud variations on the Earth's energy budget. *Nature Geoscience*, *9*(12), 871–874. https://doi.org/10.1038/ngeo2828